1 **Testing the Two-Layer Model for Correcting Near Cloud Reflectance**
2 **Enhancement Using LES/SHDOM Simulated Radiances**

3 GUOYONG WEN[1,2], ALEXANDER MARSHAK[1], TAMÁS VÁRNAI[1,3], AND ROBERT LEVY[1]

4 Short title: Near-cloud Reflectance for Aerosol Retrievals

6

[1]NASA Goddard Space Flight Center, Greenbelt, Maryland
[2]GESTAR/Morgan State University, Maryland
[3]University of Maryland Baltimore County, Baltimore, Maryland

7   Authors

8   Dr. Guoyong Wen
         NASA/Goddard Space Flight Center Code 613 & GESTAR/Morgan State University
         Greenbelt, MD 20771
         Guoyong.Wen-1@nasa.gov
         Phone: (301) 614-6220
         Fax: (301) 614-6307

         Dr. Alexander Marshak
         NASA Goddard Space Flight Center, Code 613
         Greenbelt, MD 20771
         Alexander.Marshak@nasa.gov
         (301) 614-6122

         Dr. Tamás Várnai
         NASA Goddard Space Flight Center, Code 613 &
         JCET/University of Maryland Baltimore County
         Greenbelt, MD 20771
         (301) 614-6408
         tamas.varnai@nasa.gov

         Dr. Robert Levy
         NASA Goddard Space Flight Center, Code 613
         Greenbelt, MD 20771
         Robert.C.Levy@nasa.gov
         (301) 614-6123

9 **ABSTRACT**

10 A transition zone exists between cloudy skies and clear sky, such that clouds scatter solar

11 radiation into clear sky regions. From a satellite perspective, it appears that clouds enhance the

12 radiation nearby. We seek a simple method to estimate this enhancement, since it is so

13 computationally expensive to account for all 3-dimensional (3D) scattering processes. In

14 previous studies, we developed a simple two-layer model (2LM) that estimated the radiation

15 scattered via cloud-molecular interactions. Here we have developed a new model to accounts for

16 cloud-surface interaction (CSI). We test the models by comparing to calculations provided by

17 full 3D radiative transfer simulations of realistic cloud scenes. For these scenes, the MODIS-like

18 radiance fields were computed from the Spherical Harmonic Discrete Ordinate Method

19 (SHDOM), based on a large number of cumulus fields simulated by the UCLA Large Eddy

20 Simulation (LES) model. We find that the original 2LM model that estimates cloud-air molecule

21 interactions accounts for 64% of the total reflectance enhancement, and the new model

22 (2LM+CSI) that also includes cloud-surface interactions accounts for nearly 80%. We discuss

23 the possibility of accounting for cloud-aerosol radiative interactions in 3D cloud induced

24 reflectance enhancement, which may explain the remaining 20% of enhancements. Because

25 these are simple models, these corrections can be applied to global satellite observations (e.g.

26 MODIS) and help to reduce biases in aerosol and other clear-sky retrievals.

27 **1. INTRODUCTION**

28 A transition region exists between clouds and cloud-free air [*Charlson et al.*, 2007; *Koren et*

29 *al.*, 2007]. Several recent studies have shown that there are changes in aerosol optical depth

30 (AOD) as well as aerosol particle size in this transition zone [e.g., *Su et al.*, 2008; *Loeb and*

31 *Schuster*, 2008; *Tackett and Di Girolamo*, 2009; *Twohy et al.*, 2009; *Redemann et al.*, 2009;

32   *Jeong and Li*, 2010; *Várnai and Marshak*, 2011, 2012, 2014; *Bar-Or et al.*, 2012; *Yang et al.*,

33   2014]. The transition zone is also a region where solar radiative transfer processes become

34   highly 3-dimensional (3D) [*Wen et al.*, 2008; *Kassianov and Ovtchinnikov*, 2008; *Marshak et al.*,

35   2008; *Yang and Di Girolamo*, 2008].

36   Sunlight scattered by clouds enhances the reflectance in nearby clear regions. *Wen et al.*

37   [2008] showed that Rayleigh scattering of cloud reflected sunlight is the dominant mechanism

38   for the reflectance enhancement in clear area near clouds. This 3D cloud effect is similar to the

39   adjacency effect [e.g., *Odell and Weinman*, 1975; *Otterman and Fraser*, 1979; *Kaufman*, 1979;

40   *Lyapustin and Kaufman*, 2001], however it is the cloud instead of a bright surface affecting the

41   image. The 3D cloud effects can lead to an apparent "bluing" of clear region [*Marshak et al.*,

42   2008] because of larger Rayleigh scattering in shorter wavelengths. In terms of aerosol retrieval,

43   the enhanced radiation not only creates bias in retrieving total AOD but also biases in retrieving

44   spectral dependence and interpreting relative aerosol size (via Ångstrom Exponent). Not

45   accounting for cloud 3D effects will cause incorrect interpretation of satellite-based aerosol data

46   near clouds and hence in accurately quantifying aerosol radiative effects or aerosol-cloud

47   interactions.

48   In an earlier study [*Marshak et al.*, 2008], we developed a simple two-layer model (2LM) for

49   estimating and correcting for near-cloud enhancement. This 2LM accounted for the radiative

50   interactions between boundary-layer clouds and the molecular layer of clear air above it. This

51   2LM was "validated" for a few scenes using Monte Carlo calculations [*Wen et al.*, 2007, 2008],

52   which led to *Wen et al.* [2013] applying the correction model to a full Moderate Resolution

53   Imaging Spectroradiometer (MODIS) granule. In this case, *Wen et al.,* [2013] corrected for

54   cloud-molecular interactions in the MODIS bands, and the "corrected" reflectances were then

55   used as inputs for the dark-target MODIS aerosol retrieval [*Remer et al.*, 2005; *Levy et al.*,

56   2010].

57   It is not clear whether the simple 2LM always improves MODIS aerosol retrievals. Since

58   Rayleigh scattering optical depth decreases much faster with wavelength (inversely proportional

59   to the 4th power of wavelength) than does either AOD or ocean spectral albedo, corrections only

60   for cloud-Rayleigh interactions may lead to a different kind of bias. At longer wavelengths,

61   where Rayleigh scattering is negligible, aerosol scattering and ocean reflection can be

62   substantial, especially under coarse-size aerosol or rough ocean conditions. Thus the corrections

63   for Rayleigh scattering alone skew towards shorter wavelengths [*Wen et al.*, 2013] and bias

64   aerosol retrieval.

65   Recently, *Marshak et al.* [2014] developed a new approach to overcome the shortcoming of

66   the 2LM by relating the short wavelength (e.g., 0.47 μm of MODIS) correction to longer

67   wavelengths. They found that the reflectance and the enhancements for the longer wavelength

68   were linearly correlated with to the 0.47μm band. More importantly, the linear regression

69   coefficient (i.e., the slope) relating the reflectance enhancement for a longer wavelength to that

70   for the short wavelength can be approximated by the linear regression coefficient for the

71   reflectances for the same pair of wavelengths. Note that the linear regression coefficients depend

72   on aerosol properties and the surrounding cloud structure and are computed for each MODIS 10

73   km box. Thus reflectance enhancement at longer wavelengths can be derived from the

74   enhancement at 0.47 μm. In this study, then, we focus on reflectance enhancement at 0.47 μm.

75   Two essential tasks need to be carried out in order to make the correction model as a useful

76   tool for MODIS aerosol retrievals. First, we need to reduce the bias of the 2LM alone by

77   including other 3D cloud radiative effects in addition to cloud-Rayleigh scattering interaction.

78 Second, we need to test the correction model to quantify errors in the reflectance enhancement

79 estimates.

80   In this paper, we present a new model that estimates the reflectance enhancements due to

81 cloud-surface interactions. We perform an error analysis to the models by comparing the model-

82 estimated reflectance enhancements to the truth computed by the Spherical Harmonic Discrete

83 Ordinate Method (SHDOM) [*Evans*, 1998] for a large number of cumulus cloud fields generated

84 from UCLA Large Eddy Simulation (LES) model [*Stevens et al.*, 1999] and GEOS-5 aerosol

85 profiles. This approach is similar to those of *Yang and Di Girolamo* [2008] and *Marshak et al.*

86 [2014] in studying 3D radiative effects for satellite remote sensing.

87   Section 2 briefly reviews the 2LM and presents the method of accounting for cloud-surface

88 interactions. The data of LES/SHDOM simulations are described in section 3. The error analyses

89 are presented in Section 4, along with discussion of the possibility to account cloud-aerosol

90 radiative interactions, which is followed by a summary section.

91 **2. TWO MODELS FOR CLEAR SKY ENHANCEMENT DUE TO NEARBY CLOUDS**

92   Sunlight scattered by broken clouds enhances diffuse solar radiation in the clear area in the

93 vicinity of clouds. Subsequent scattering of the diffuse sunlight by air molecules, aerosols, and

94 surface leads to the enhancement of clear column reflectance. 3D clouds also cast shadows to

95 decrease the reflectance in nearby clear areas [e.g., *Di Giuseppe and Tompkins*, 2003], and

96 methods have been developed to discriminate cloud shadows for MODIS remote sensing [e.g.,

97 *Ackerman et al.*, 1998; *Remer et al.*, 2005]. In this paper, we consider only the enhancement

98 effects of clouds. We first briefly review the 2LM developed earlier for correcting clear-air

99 reflectance enhancement due to cloud-air molecule interactions [*Marshak et al.*, 2008]. Then we

100 present a method for also accounting for cloud-surface radiative interactions.

2.1. THE TWO-LAYER MODEL (2LM) FOR CLOUD-AIR MOLECULE INTERACTIONS

Fig. 1a sketches the 2LM that estimates clear-air reflectance enhancement due to the radiative interactions between a cloud layer with cloud albedo α_c and the overlaying molecular atmosphere with scattering optical depth of τ_m. In this model, the clear-air reflectance enhancement is the result of cloud-reflected upward radiation being scattered by the molecular layer into the direction of the satellite sensor.

In the two-layer system, we consider the processes that affect radiation reflected from clouds as it travels through the molecular layer above. These radiative transfer processes include scattering and extinction by air molecules, and multiple reflections between the cloud layer and the molecular layer above it. To derive an analytical approximation for the cloud-induced reflectance enhancement, we consider two reflectances for the two-layer system. One is the reflectance from a broken cloud field with a scattering molecular layer above it. This reflectance includes both scattered radiation and cloud reflected radiation attenuated by molecular scattering. The other is second component in the first reflectance (i.e., the reflected radiation from the same broken cloud field but with the molecules in the upper layer causing extinction) [*Marshak et al.*, 2008]. The difference between the two reflectances yields the reflectance scattered to the sensor, or the reflectance enhancement. Both reflectances may be expressed analytically as described below.

Generated by the cloud reflected upward flux, the first reflectance (r_1) is simply the total TOA reflectance that includes molecular scattering, extinction, and multiple reflections between two layers. Generated by the same upward flux, the second reflectance (r_2) is the non-scattered radiance with the molecular layer causing only extinction. The expressions for the two reflectances are shown in Eq. (1):

124 $$r_1(\lambda,\Omega,\Omega_0) = \frac{\alpha_c T_m(\tau_m(\lambda),\Omega_0) T_{m,diff}(\tau_m(\lambda),\Omega)}{1 - \alpha_c R_m(\tau_m(\lambda))},$$ (1a)

125 $$r_2(\lambda,\Omega,\Omega_0) = \frac{\alpha_c T_m(\tau_m(\lambda),\Omega_0) T_{m,beam}(\tau_m(\lambda),\Omega)}{1 - \alpha_c R_m(\tau_m(\lambda))}.$$ (1b)

126 where α_c is cloud albedo, $\tau_m(\lambda)$ is the molecular scattering optical depth above cloud top level

127 for wavelength λ, Ω_0 and Ω are the directions to the Sun and the satellite, T_m and $T_{m,diff}$ are

128 transmittances of the molecular layer for collimated sunlight from above and diffuse radiation

129 reflected from the cloud layer below, respectively, R_m is the reflectance of the molecular layer for

130 upwelling radiation from the cloud layer, and $T_{m,beam} = \exp(-\tau_m(\lambda)/\mu)$ is the beam transmittance of

131 the molecular layer for upwelling radiation from the cloud layer, where μ is the cosine of the

132 satellite viewing zenith angle (VZA). (See Table I in *Wen et al.*, 2013, for the detailed definition

133 of each term.)

134   The difference between the two reflectances gives the molecule-scattered reflectance in the

135 two-layer system or cloud-induced reflectance enhancement (ΔR_m), as shown in Eq. (2)

136 $$\Delta R_m(\lambda,\Omega,\Omega_0) = \frac{\alpha_c T_m(\tau_m(\lambda),\Omega_0)}{1 - \alpha_c R_m(\tau_m(\lambda))}\left[T_{m,diff}(\tau_m(\lambda),\Omega) - T_{m,beam}(\tau_m(\lambda),\Omega)\right].$$ (2)

137 Fig. 1b shows schematically the characteristics of the 2LM versus the real enhancement. For a

138 given viewing angle, the reflectance enhancement is approximately a linear function of the 1D

139 cloud albedo α_c since the contribution from multiple reflections is small (see Eq. (2)). As we will

140 see in Section 4, the true enhancement is not a linear function of 1D cloud albedo; it increases

141 quickly for small cloud albedos and gradually saturates for large cloud albedos. For small cloud

142 albedos, the 2LM underestimates the truth because it does not account for cloud-surface and

143 cloud-aerosol interactions. For large cloud albedos, the 2LM enhancement estimates continue to

144 increase linearly with cloud albedo, which overestimates the non-linear (saturated) enhancement.

145   The input for the 2LM includes cloud scene albedo, molecular optical depth above clouds,

146   solar zenith angle (SZA), and satellite viewing geometry. The average cloud scene albedo in

147   each 10 km x 10 km box is estimated using the plane-parallel independent pixel approximation

148   (IPA) by averaging the albedo for each 500 m pixel computed using cloud optical depths

149   provided in LES/SHDOM simulation data. The transmittances and reflectance of the molecular

150   layer are calculated as a function of the known cloud-top height. In practice, cloud albedo may

151   be estimated using broadband to narrowband conversion method [*Wen et al.*, 2013], and MODIS

152   cloud-top height [*Platnick et al.*, 2003] can be used to compute molecular layer reflectance and

153   transmittances.

154   **2.2. CLOUD-SURFACE RADIATIVE INTERACTIONS (CSI)**

155   Sunlight scattered by broken clouds increases the downward diffuse radiative flux in nearby

156   clear areas and subsequently leads to the reflectance enhancement through surface reflection and

157   atmospheric extinction. Thus the reflectance enhancement (ΔR_s) due to cloud-surface radiative

158   interactions (CSI) may be expressed as

159    $$\Delta R_s = T_{clear} \alpha_s e^{-\frac{\tau}{\mu}}, \qquad\qquad (3),$$

160   where T_{clear} is the cloud-induced clear area diffuse transmittance (i.e., the extra radiation that

161   reaches a surface area because of sideways scattering by clouds), α_s the surface albedo, τ the

162   atmospheric optical depth (aerosol and molecular scattering), μ the cosine of VZA.

163   Here, we use a one-layer, stochastic Poisson model to model the downward diffuse radiative

164   flux from a broken cloud field [*Titov*, 1990; *Kassianov*, 2003; *Zhuravleva and Marshak* 2005].

165   The second simulation of satellite signal in the solar spectrum (6S) model [*Vermote et al.*, 1997],

166   the same one used for SHDOM simulation, is used to compute surface albedo. The Poisson

167   model [*Titov*, 1990] assumes that for a given cloud fraction clouds are distributed uniformly in a

168   unit volume. For statistically homogeneous cloud fields, a closed system of equations is derived

169   for average intensity, and the closed equations are solved using Monte Carlo method. While this

170   Poisson model can be generalized to multi-layers [e.g., *Kassianov*, 2003], and compared with

171   fractal cloud model for radiative flux computation [*Zhuravleva and Marshak*, 2005], we use the

172   one-layer Poisson model in this study.

173   The Poisson model is completely determined by cloud fractional cover (*f*), cloud geometric

174   thickness *H*, average horizontal size of clouds *D*, and averaged cloud optical properties,

175   including cloud optical depth, single scattering albedo and scattering phase function. For a fixed

176   cloud thickness the cloud aspect ratio defined as the ratio of cloud horizontal to vertical extent

177   (*D/H*) is used as input parameter. For given inputs of cloud properties and solar zenith angle, the

178   Poisson model computes the domain average albedo, absorption, and transmittances for both

179   direct and diffuse radiation.

180   To calculate cloud-induced diffuse transmittance, we use the following approximation. First,

181   we assume that the domain average diffuse transmittance ($T_{3D,cloudy}$) is a fractional area-weighted

182   sum of clear and cloudy diffuse transmittances (T_{clear} and T_{cloud}),

183        $T_{3D,cloudy} = fT_{cloud} + (1-f)T_{clear}$ (4)

184   where $T_{3D,cloudy}$ is computed by the stochastic Poisson model for a broken cloud field and T_{cloudy}

185   is computed from the plane parallel approximation. From here the clear sky diffuse transmittance

186   can be estimated as

187        $T_{clear} = \left(T_{3D,cloudy} - fT_{cloud}\right)/(1-f)$.   (5)

188   Assuming a cloud aspect ratio of 2, Fig. 2 plots the Poisson model-computed clear-sky

189   diffuse transmittance as a function of broken cloud field albedo. Each point represents a different

190 cloud fraction and average cloud optical depth (COD). There are some notable distinctive

191 features. For a given cloud fraction, the diffuse transmittance increases rapidly with for small

192 CODs, reaches local maxima, and then decreases gradually. For a given cloud optical depth, the

193 diffuse transmittance increases with cloud fraction, reaching 0.25-0.30 for a broken cloud field

194 albedo greater than 0.25.

195 We have run the Poisson model for a discrete values of cloud properties and solar

196 geometries, thus creating lookup tables (LUTs) of diffuse transmittance. Together with the ocean

197 albedo computed from the ocean reflection model and atmospheric extinction, we are able to

198 estimate the enhancement due to cloud-surface radiative interaction.

199 **3. DATA**

200 Our study considers the radiation fields for cumulus cloud scenes over oceans. LES model

201 was used to generate 26 cumulus cloud fields. Initialized using meteorological profiles

202 (temperature, water vapor, wind components and vertical velocity) from the ERA-Interim

203 reanalysis [*Dee et al.*, 2011], the LES runs were performed with a domain size of 20 km x 20

204 km, with a horizontal grid spacing of 62.5 m and a variable vertical grid with 59 to 102 levels

205 with vertical resolution of 40 m or less. Each simulation started at 06:00 local time and lasted for

206 8 hours. The LES cloud microphysics assumes a fixed cloud droplet concentration and uses a

207 two-moment drizzle/rain bulk microphysics scheme. The cloud droplet concentration was chosen

208 randomly from an exponential distribution between 40 cm^{-3} and 400 cm^{-3}. The LES shortwave

209 and longwave radiative cooling/heating rates were calculated using the Fu/McISA [*Pincus and*

210 *Stevens*, 2009] independent column approximation radiative transfer code. An example of LES

211 cloud optical depth field and computed 1D albedo is presented in Fig. 3.

212 For 3D radiative computation, the cloud field for a single time (6 hr or 12:00 pm local time)

213 was chosen for each of the 26 LES simulation. Fig. 4a show cloud properties of the 26 LES

214 clouds. The 26 LES cloud fields were combined with 40 representative aerosol profiles. Out of

215 26 LES cloud fields, 24 fields were combined with 3 different aerosol profiles, and 2 fields with

216 4 different aerosol profiles to make 80 different cloud/aerosol scenes. In other words, each of the

217 40 aerosol profiles was used with two different cloud scenes to make 80 different cloud/aerosol

218 scenes.

219 These aerosol profiles were obtained from GEOS-5 [*Rienecker et al.*, 2011] global fields

220 over tropical and mid-latitude oceans. GEOS-5 has five aerosol types: dust, sea salt, sulfate,

221 black carbon, and organic carbon [*Chin et al.*, 2002; *Colarco et al.*, 2010]. Aerosol optical

222 properties were calculated from the GEOS-5 optical property tables as a function of LES relative

223 humidity. Thus aerosol optical properties vary horizontally and vertically in space. The 40

224 aerosol profiles have a wide range of aerosol properties as shown in Fig. 4b.

225 The radiances for these 80 scenes were calculated with SHDOM at the LES resolution for the

226 seven MODIS bands used for aerosol remote sensing (wavelengths of 0.466, 0.553, 0.646,

227 0.855,1.243, 1.632, and 2.119 μm) [*Remer et al.*, 2005]. Rayleigh molecular scattering and

228 molecular absorption from water vapor and ozone were included up to the 15.6 km domain top.

229 An SHDOM ocean surface reflectance model with the LES surface wind speed was assumed.

230 The solar-viewing geometry was obtained for the LES latitude, date, and the 13:30 local time of

231 the Aqua overpass. SHDOM runs were made for 3D cloud/aerosol fields (i.e., MODIS-like), 3D

232 hydrated aerosol-only fields, and 1D aerosol-only fields. For 3D cloud/aerosol fields and 3D

233 hydrated aerosol-only fields, aerosol optical properties respond to the LES relative humidity

234 through aerosol hydration and vary horizontally and vertically in space. For 1D aerosol-only

235 fields, the horizontally averaged outside-cloud relative humidity is used to compute aerosol

236   optical properties. In this study, the true reflectance enhancement (ΔR_{truth}) is defined as the

237   difference between reflectances for the 3D cloud/aerosol fields and the 3D hydrated aerosol-only

238   fields.

239   The standard MODIS aerosol retrieval [*Levy et al.*, 2013] uses input observations at 500 m

240   spatial resolution (nominal at nadir view) to derive aerosol properties at 10 km resolution.

241   Therefore, we averaged the SHDOM results (the 3D cloud/aerosol reflectance fields for cloudy

242   and the 3D hydrated aerosol-only reflectance fields for clear) to provide 500 meter resolution

243   MODIS-like data in the seven wavelengths. To account for the variability of global observing

244   geometry, these values were calculated for 23 viewing directions with zenith angles every 6°

245   from 0° to 66°. Note, that the upper bound in the model configuration is 15 km, rather than 700

246   km observation of MODIS. Within scene (20 km x 20 km) variation in viewing and solar angles

247   are ignored. Thus for each MODIS band, there are 1840 (80 cloud/aerosol scenes times 23

248   viewing directions) radiance images. These scenes would be broken into 10 km x 10 km boxes of

249   500 m pixels, following the strategy of the MODIS aerosol retrieval.

250   The MODIS aerosol retrieval performs upon clear (non-cloud) pixels. Following the cloud-

251   masking scheme of operational MODIS dark target aerosol retrievals [*Martins et al.*, 2002;

252   *Remer et al.*, 2005; *Levy et al.*, 2010], we identified clear pixels within each 10 km x 10 km box

253   of each of the 1840 MODIS-like cloud/aerosol scenes. Overall, 100188 of the 500 m pixels and

254   associated 3154 of the 10 km boxes passed the test. Note that more clear pixels passed MOD04

255   test for nadir viewing direction than that for oblique viewing angles (Fig. 2c), and that the Aqua

256   satellite has a local equatorial crossing time approximately 1:30 pm. Therefore, the results in this

257   study are biased slightly towards higher sun and lower viewing zenith angles.

4. RESULTS

258

259   We test our models by comparing the estimated reflectance enhancements to the truth. We

260   test (1) the 2LM that accounts for cloud-molecule radiative interactions to estimate ΔR_m, and (2)

261   the 2LM+CSI that accounts for cloud-molecule and cloud-surface radiative interactions to

262   estimate $\Delta R_m + \Delta R_s$. First we show an example of 2LM. Then we present results for the two

263   models, followed by a discussion of possibility to account for cloud-molecule, cloud-surface, and

264   cloud-aerosol radiative interactions in a model called 2LM+CSI+CAI.

4.1. AN EXAMPLE FOR 2LM

265

266   We compared 2LM with the truth for the cloud field in Fig. 3a as an example. Fig. 5 shows

267   the view-angle dependence of reflectance enhancements for the four 10 km x 10 km sub-images

268   of the cloudy scene in Fig. 3a. The true reflectance enhancements are in color, and those for 2LM

269   are in black. A distinctive feature of the true reflectance enhancement is its view-angle

270   dependence. It is evident that the true reflectance enhancement increases with view angle, and

271   that 2LM also captures, to some extent, this dependence.

272   Another remarkable feature of the 2LM is that its reflectance enhancements for the four 10

273   km x 10 km boxes are very different from one another. This is due primarily to the dependence

274   of the 2LM reflectance enhancement on cloud albedo, for cloud-top height is less variable for

275   cumulus clouds (see Eq. (2)). Starting counter-clockwise from the upper left corner (Fig. 5a), the

276   increase of average 2LM enhancement (0.0028, 0.0045, 0.0049, 0.0069 in Fig. 5) is evidently

277   associated with increase in cloud field albedo (0.05, 0.07, 0.08, 0.12 in Fig. 3b).

278   Unlike the 2LM enhancement, the true reflectance enhancement does not have a clear

279   dependence on the 1D cloud albedo because, in reality, it is a result of a non-linear 3D radiative

280   transfer interaction between cloud and clear air. The true scene albedo of a 10 km x 10 km box is

14

281   not a unique function of cloud optical properties either, and is strongly affected by cloud-field

282   structure [*Marshak et al.,* 1995]. Furthermore, the true enhancement calculations also account for

283   the hydrated aerosols that vary in 3D space. As a result, the true reflectance enhancement is more

284   variable than its 2LM counterpart.

285   The errors in 2LM reflectance enhancement for each 10 km x 10 km box vary from scene to

286   scene, and can be relatively large and view angle dependent. For example, for the two boxes on

287   the right side of Fig. 3a, the error is about 10%. However, for the upper-left box in Fig. 3a, the

288   error ranges from -0.003 (-50%) for nadir direction to -0.006 (-60%) for the oblique viewing

289   angle of 48° (black dots minus colors in Fig. 5a). For the 20 km x 20 km domain and viewing

290   angle average, the error in 2LM enhancement is about -31%, which differs tremendously form

291   the error for each 10 km x 10 km boxes. Thus, it is important to compare the statistics of

292   modeled reflectance enhancements to the truth, as described in the following sections.

293   **4.2. 2LM FOR CLOUD-AIR MOLECULE INTERACTIONS**

294   Figure 6 compares the 2LM reflectance enhancements with the true enhancement values for

295   different view angles for all scenes as a function of 1D cloud scene albedo. It is clear that both

296   modeled and the true reflectance enhancements increase with cloud albedo for a given viewing

297   angle. However, there are some remarkable differences between the two as the sketched in Fig.

298   1b. As expected from Eq. (2), for a given view-angle, the 2LM reflectance enhancement is a

299   linear function of cloud albedo. In reality, the enhancement is a non-linear function of the 1D

300   cloud albedo. The true enhancement increases rapidly for small cloud albedos, and saturates at

301   the larger ones. The true enhancement is always larger and more variable than its model

302   counterpart for albedos smaller than 0.15. However, for albedos larger than 0.15, for some cases

303   the true enhancement is smaller than its 2LM estimate.

304   The 2LM underestimates the true enhancement at least for albedo smaller than 0.15 because

305   it lacks contributions from cloud-surface and cloud-aerosol radiative interactions. The

306   overestimate of the enhancement for large 1D cloud albedos is primarily the result of the

307   application of the simple linear model to situations when the non-linearity of radiative transfer is

308   pronounced. This also suggests the limitation of the 2LM for larger cloud albedos or cloud

309   optical depth and cloud fraction.

310   Fig. 7a compares the average and standard deviation of 2LM estimated reflectance

311   enhancements with the truth as a function of cloud scene albedo. There are 104 different albedo

312   values and 3154 radiances for 10 km x 10 km boxes. The latter is the result of the same number

313   of broken cloud scenes with different combinations of aerosol profiles and viewing angles. Thus

314   there are 104 average reflectance enhancements corresponding to each individual cloud albedo,

315   for both 2LM and the truth. The error bars show the standard deviation of scene-average

316   enhancement values due to different view direction for 2LM and additional variation in aerosol

317   properties for the truth.

318   Similar to those for different VZA in Fig. 1b and Fig. 6, both modeled and true average

319   reflectance enhancements increase with cloud albedo. The 2LM average reflectance

320   enhancement increases rather linearly while the true average enhancement has a much bigger

321   dynamic range for each value of cloud field albedo. Again, we clearly see that 2LM

322   underestimates the true enhancement at least for albedo smaller than 0.15.

323   The standard deviation of 2LM reflectance enhancement for a given cloud albedo is much

324   smaller than the truth. This is because, for a given cloud field, the 2LM reflectance enhancement

325   only varies with viewing angle, while the true enhancement, in addition to viewing geometry,

326   depends on the 3D radiative transfer process and variable aerosol properties. As a result, the

327   mean values of the 104 average enhancements and the standard deviations are smaller for the

328   2LM (0.0038 and 0.0003, respectively) than that for the truth (0.0055 and 0.0009, respectively).

329   On average, the cloud-air molecule interaction accounts for about 70% of the 3D enhancement,

330   which is consistent with the results of *Wen et al.* [2008]. In other words, the 2LM reflectance

331   enhancement is biased low by 30%.

332   Next we compare the averages and standard deviation of the 2LM enhancements with the

333   truth for different mean cloud optical depths (Fig. 7b) and different cloud fractions (Fig. 7c).

334   There are 317 unique average cloud optical depths and 88 different cloud fraction values. For

335   both 2LM and the truth, the average enhancement increases with average cloud optical depth and

336   cloud fraction. This is similar to Fig. 7a because cloud scene albedo, average cloud optical depth,

337   and cloud fraction are positively correlated. Compared to the true values, the 2LM average

338   enhancement increases more linearly with either cloud optical depth or cloud fraction. Similarly

339   to Fig. 7a, the model underestimates the mean and standard deviation of the enhancements

340   except for a few cases for large enough cloud optical depths and cloud fractions.

341   It is important to note that the 2LM already overestimates the enhancement for large cloud

342   field albedos (cloud optical depth, and/or cloud fraction). The critical values of cloud albedo

343   (0.1) and cloud fraction (0.6) were determined empirically; no further correction for cloud-

344   surface radiative interactions will be made for cloud fields with an albedo higher than 0.1 or

345   cloud fraction larger than 0.6 in 2LM+CSI.

346   **4.3. 2LM+CSI FOR CLOUD-AIR MOLECULE AND CLOUD-SURFACE RADIATIVE INTERACTIONS**

347   2LM accounts about 70% of the true reflectance enhancement. Here we show that the 2LM

348   can be further improved when additional cloud-surface interactions are included in 2LM+CSI.

349   Similar to Fig. 7a, Fig. 8a compares the enhancements for 2LM+CSI as a function of cloud

350   field albedo. It is clear that including cloud-surface interactions improves the model estimates of

351   the reflectance enhancement for cloud field albedos less than 0.1. For 2LM+CSI, the mean value

352   of average reflectance enhancement is 0.0046 compared to 0.0038 for 2LM. As a result, the

353   2LM+CSI (cloud-air molecule and cloud-surface interactions) accounts for 84% of the true

354   enhancement of 0.0055. The bias in 2LM+CSI is about 16% compared to 30% for 2LM. Note

355   the 2LM+CSI does not change the typical standard deviation. The comparison between the

356   2LM+CSI and the true enhancements as a function of cloud optical depth and cloud fraction is

357   also shown in Figs. 8b and 8c, respectively.

358   The improvement of the models may be seen from scatter plots in Fig. 9, with different cloud

359   fractions indicated by colors. As expected, the model-estimated enhancement increases with

360   cloud fraction. Note that 2LM+CSI does not apply to cloud fields with cloud fractions bigger

361   than 0.6. Straight lines are fitted to the scatter plot through the origin. Evidently, the slope

362   increases from 0.58 for 2LM, to 0.73 for 2LM+CSI, showing the improvement when cloud-

363   surface radiative interactions are accounted for in the 2LM.

364   **4.4. STATISTICAL DISTRIBUTIONS OF ERRORS IN MODEL ESTIMATES**

365   Finally, we examine the error distribution in the model-estimated reflectance enhancements.

366   In the error distribution for 2LM (Fig. 10a), the median, mean, and standard deviation are -

367   0.0013, -0.0018, and 0.0017, respectively. The majority of the differences between the 2LM

368   enhancement values and the true ones are negative and only 4% of values are positive.

369   Comparing with the average true reflectance enhancement of 0.00496 (Fig. 11), we find that

370   overall average of 2LM is biased low by about 36%, slightly more than they were for different

371 cloud properties in Figure 7. Also, the magnitude of the standard deviation is as large as the

372 magnitude of the mean value.

373 The error distribution for 2LM+CSI (Fig. 10b) has a median, mean, and standard deviation of

374 -0.0007, -0.0010, and 0.0015, respectively. In the distribution, 23% of values are greater than

375 zero, compared with 4% for 2LM. From 2LM to 2LM+CSI, overall statistical bias error reduced

376 by half from -0.0018 to -0.0010. The standard deviation is slightly smaller for 2LM+CSI than for

377 2LM. The bias error is reduced from -36% for 2LM to -20% for 2LM+CSI.

378 Fig. 11 compares the frequency distribution of 2LM+CSI estimated reflectance enhancement

379 with the truth. We find that the frequency distribution for 2LM+CSI largely resembles that for

380 the truth. The median, mean, and standard deviation for 2LM+CSI are 0.00315, 0.00390, and

381 0.00234 compared to 0.00418, 0.00496, and 0.00301 for the truth. For overall statistics, the

382 2LM+CSI accounts for ~80% of the enhancement.

383 **4.5. DISCUSSION OF CLOUD-AEROSOL INTERACTIONS**

384 Similarly to cloud-surface radiative interactions, cloud-induced diffuse radiation scattered by

385 aerosol also enhance clear column reflectance. However, the reflectance enhancement (ΔR_a) due

386 to cloud-aerosol radiative interactions is much more difficult to estimate, since the enhancement

387 not only depends on the cloud-induced diffuse radiation but also on unknown aerosol properties;

388 moreover, it depends on the unknown distribution of scattering angle in the process of radiative

389 interactions between clouds and aerosols. Still, the contribution of cloud-aerosol radiative

390 interactions may be approximately estimated. Here we show that the concept of the 2LM

391 developed for cloud-air molecule radiative interactions can also be useful for estimating cloud-

392 aerosol interactions.

393   Consider the top layer in the 2LM consisting of air molecules and aerosols. We cannot

394   simply include aerosol effects by adding AOD to the molecular optical depth in the 2LM because

395   the aerosol scattering phase function is much more variable than that for molecular scattering,

396   and strongly depends on the unknown scattering angle. In order to somehow account for aerosols

397   in the 2LM, we can use the single scattering approximation.

398   We consider the reflectance for a layer consisting of molecules and aerosols. In a single

399   scattering approximation, the reflectance is proportional to optical depth, single scattering

400   albedo, and scattering phase function, i.e.

401     $$r(\theta,\theta',\phi-\phi') = \tau_m P_m(\mu_{scat})/(4\mu\mu') + \omega_a \tau_a P_a(\mu_{scat})/(4\mu\mu').$$ (6)

402   Here τ_m and P_m are molecular optical depth and scattering phase function, ω_a, τ_a, P_a are aerosol

403   single scattering albedo, optical depth and scattering phase function, $\mu=\cos(\theta)$ and $\mu'=\cos(\theta')$ are

404   cosines of the viewing and incident zenith angles (θ and θ'), ϕ and are ϕ' are azimuth angles, and

405   μ_{scat} is cosine of the effective scattering angle [*Hansen and Travis*, 1974; *Kaufman et al.*, 1997].

406   Eq. (6) may also be expressed as

407     $$r(\theta,\theta',\phi-\phi') = \tau_{m,eff} P_m(\mu_{scat})/(4\mu\mu'),$$ (7a)

408   where the effective molecular scattering optical depth $\tau_{m,eff}$ is

409     $$\tau_{m,eff} = \tau_m + \varepsilon\tau_a$$ (7b)

410   and

411     $$\varepsilon = \omega_a P_a(\mu_{scat})/P_m(\mu_{scat}).$$ (7c)

412   The scale factor ε accounts for the phase function difference between molecular and aerosol

413   scattering at the μ_{scat}. Thus one can get a rough estimate of the total enhancement due to cloud-

414   aerosol and cloud-air molecule radiative interactions using the same molecular scattering

415   equation by adding a scaled optical depth to the molecular optical depth.

416   Figure 12 shows the phase function ratios for the 40 aerosol types. The phase function ratio

417   has a peak in the forward direction. The ratio is less than one for a large range of scattering

418   angles and has minimum value around 0.1-0.2. To demonstrate the possible magnitude of

419   reflectance enhancement contributions from cloud-aerosol interactions, we use the AOT values

420   provided in the data set and assume a small value of 0.2 for ε. The result is presented in Fig. 13.

421   Note that, similarly to 2LM+CSI, the enhancement due to cloud-aerosol interactions induced

422   enhancement is not computed for cloud field albedos larger than 0.1 or for cloud fraction larger

423   than 0.6. The figure shows that the 2LM including additional cloud-aerosol radiative interactions

424   can accounts for 90% of the enhancement for this somewhat arbitrary small ε.

425   Here we used a somewhat arbitrary ε and AOT values in the data set to demonstrate a rough

426   magnitude of the reflectance enhancement due to cloud-aerosol interactions. In real application,

427   Monte Carlo simulations could provide the parameter ε as a function of aerosol and cloud

428   properties and Sun-view geometry, and the MODIS retrieved AOT may be used as a first

429   approximation for estimating the enhancement.

430   **5. SUMMARY AND DISCUSSION**

431   We developed a new model to account for cloud-surface interactions that make significant

432   contributions to clear sky reflectance enhancements in broken cloud fields. In the new method,

433   the cloud-surface radiative interactions are accounted for by using an existing Poisson model of

434   cloud spatial distribution [*Titov*, 1990] to estimate cloud-induced downward diffuse radiative

435   flux at the surface. The radiative transfer computation for Poisson cloud fields is efficient to

436   provide sufficiently accurate domain average fluxes [*Zhuravleva and Marshak*, 2005]. This

437 model can be applied for operational processing for correcting reflectance enhancement due to

438 cloud-surface radiative interaction for MODIS aerosol retrieval.

439 We further assessed the accuracy of two models. The first one is the 2LM that accounts only

440 for cloud-air molecule radiative interactions. The second model, or 2LM+CSI, accounts for both

441 cloud-air molecule and cloud-surface radiative interactions. We tested these models to quantify

442 errors in the reflectance enhancement estimates using the true radiances calculated by SHDOM

443 [*Evans*, 1998] for 80 cloud/aerosol scenes from LES [*Stevens et al.*, 1999]. We demonstrated that

444 the true reflectance enhancement has clear view angle dependence, and that 2LM (the model that

445 accounts for cloud-air molecule interactions only) captures much of this dependence. While the

446 2LM enhancement for each individual image may have large errors, on average 2LM results are

447 reasonable.

448 Detailed analyses show that, for a given viewing angle, 2LM estimated enhancement

449 increases linearly with the 1D cloud field albedo. The true enhancement increases nonlinearly

450 with the cloud field albedo: it increases rather quickly for small albedos and then becomes

451 saturated for large albedos. The 2LM enhancements are smaller and less variable compared to

452 the truth except for a few cases with large cloud albedos, cloud optical depth, or cloud fractions

453 indicating the limitation of the 1D model for those clouds. The mean error of 2LM for average is

454 -36%.

455 We performed detailed analysis to the reflectance enhancement from the model that accounts

456 for both cloud-air molecule and cloud-surface interactions (2LM+CSI). We found that the mean

457 value of the enhancement increased from 64% of the true value for 2LM to 80% for 2LM+CSI.

458 In other words, the mean error is reduced from -36% for 2LM to -20% for 2LM+CSI. Thus,

459 including cloud-surface radiative interactions in 2LM+CSI has made significant improvement to

460 the 2LM.

461   It is important to note that the 2LM is a simple model. It uses the plane-parallel

462 approximation to compute cloud albedos used for estimating the reflectance enhancements due to

463 cloud-air molecule interactions. In reality, cloud albedo in a 10 km x 10 km box is not a unique

464 function of its optical properties and can also be affected by clouds in neighboring boxes.

465 Without considering 3D radiative transfer, the plane-parallel assumption can introduce large

466 errors in estimating albedo and associated reflectance enhancement for a given cloudy scene. On

467 average, however, the model performed reasonably well estimating the true enhancement when

468 only cloud-air molecular radiative interactions are accounted for.

469   Similarly, the stochastic Poisson model is expected to provide statistically accurate fluxes.

470 For a given cloudy scene, however, the model may have large errors due to both the stochastic

471 nature of the model and the plane-parallel assumption used in deriving the clear sky diffuse flux.

472 However, the error in surface-associated reflectance enhancement is expected to be small

473 compared to that due to the plane-parallel assumption in computing 2LM reflectance

474 enhancement because cloud-surface interaction is not the largest contribution to the reflectance

475 enhancement. Nevertheless, the Poisson model is efficient in estimating the clear sky downward

476 diffuse flux needed for computing the enhancement due to cloud-surface radiative interactions.

477   We have discussed the possibility of accounting for cloud-aerosol interactions in the 2LM.

478 We demonstrated that the bias in enhancement estimate may be further reduced by introducing

479 an effective molecular optical depth for cloud-aerosol radiative interactions and using a

480 somewhat arbitrary parameter ε. Here we used AOT values provided in our data set. In reality

481 the AOT may be estimated using MODIS product as a first order approximation. The parameter

482 ε may be empirically estimated using aerosol information obtained from satellite observation and

483 Monte Carlo simulations.

484   This study focuses on the 2LM for the MODIS aerosol band at 0.47 μm. In contrast,

485 operational MODIS aerosol retrievals rely on spectral reflectances measured at seven

486 wavelengths. Recently, a new method was developed to relate the enhancement at a short

487 wavelength to those at longer wavelengths [*Marshak et al.*, 2014]. Combining the 2LM for a

488 short wavelength such as 0.47 μm with the method for longer wavelengths, we plan to perform

489 further analysis to assess errors in 2LM estimates of spectral reflectance enhancements, and to

490 test the way using these two models would affect MODIS aerosol retrievals.

492 **REFERENCES**

493 Ackerman, S. A., K. I. Strabala, W. P. Menzel, R. A. Frey, C. C. Moeller, and L. E. Gumley

494   (1998), Discriminating clear sky from clouds with MODIS, *J. Geophys. Res.*, 103(D24),

495   32,141−32,157, doi:10.1029/1998JD200032.

496 Bar-Or, R. Z., I. Koren, O. Altaratz, and E. Fredj (2012), Radiative properties of humidified

497   aerosols in cloudy environment, *Atmos. Res.*, 118, 280–294.

498 Charlson, R. J., A. S. Ackerman, F. A-M. Bender, T. L. Anderson, and Z. Liu (2007), On the

499   climate forcing consequences of the albedo continuum between cloudy and clear air, *Tellus*,

500   **59**, 715-727.

501 Chin, M., P. Ginoux, S. Kinne, O. Torres, B.N. Holben, B.N. Duncan, et al. (2002), Tropospheric

502   aerosol optical thickness from the GOCART model and comparisons with satellite and

503   sunphotometer measurements, *J. Atmos. Sci.*, 59:461−83.

504   Colarco, P., A. da Silva, M. Chin, T. Diehl (2010), Online simulations of global aerosol

505   distributions in the NASA GEOS4 model and comparisons to satellite and ground-based

506   aerosol optical depth, *J. Geophys. Res.*, 115:D14207.

507   Dee, D.P. et al. (2011), The ERA-Interim reanalysis: configuration and performance of the data

508   assimilation system, *Q. J. R. Meteorol. Soc.* **137**: 553–597. DOI:10.1002/qj.828.

509   Di Giuseppe, F., and A. M. Tompkins (2003), Three-dimensional radiative transfer in tropical

510   deep convective clouds, *J. Geophys. Res.*, 108(D23), 4741, doi:10.1029/2003JD003392.

511   Evans, K. F. (1998), The Spherical Harmonics Discrete Ordinate Method for Three-Dimensional

512   Atmospheric Radiative Transfer, *J. Atmos. Sci.*, **55**, 429-446.

513   Hansen, J. E. and L. Travis (1974), Light scattering in planetary atmosphere, *Space Science

514   Reviews*, **16**, 527-610.

515   Jeong, M. J. and Z. Li (2010), Separating real and apparent effects of cloud, humidity, and

516   dynamics on aerosol optical thickness near cloud edges, *J. Geophys. Res.*, 115, D00K32,

517   doi:10.1029/2009JD013547, 2010.

518   Kassianov, E. (2003), Stochastic radiative transfer in multilayer broken clouds. Part I: Markovian

519   approach, *J. Quant. Spectrosc. Radiat. Transfer*, 77, 373– 394, doi:10.1016/S0022-

520   4073(02)00170-X.

521   Kassianov, E. I., and M. Ovtchinnikov (2008), On reflectance ratios and aerosol optical depth

522   retrieval in the presence of cumulus clouds, *Geophys. Res. Lett.*, 35, L06807,

523   doi:10.1029/2008GL033231.

524   Kaufman, Y. J. (1979), Effect of the Earth atmosphere on contrast for zenith observation, *J.

525   Geophys. Res.*, 3165-3172, DOI: 10.1029/JC084iC06p03165.

526 Kaufman, Y.J., D. Tanre, L. Remer, A. Chu, E. Vermote, A. Chu, and B. N. Holben (1997),

527   Operational remote sensing of tropospheric aerosol over land from EOS Moderate Resolution

528   Imaging Spectroradiometer, *J. Geophys. Res.*, *102*, 17051-17067.

529 Koren, I., L. A. Remer, Y. J. Kaufman, Y. Rudich, Y., and J. V. Martins (2007), On the twilight

530   zone   between   clouds   and   aerosols,   *Geophys.   Res.   Lett.*,   34,   L08805,

531   doi:10.1029/2007GL029253.

532 Levy, R.C., L.A. Remer, R.G. Kleidman, S. Mattoo, C. Ichoku, R. Kahn, and T.F. Eck (2010),

533   Global evaluation of the Collection5 MODIS dark-target aerosol products over land, *Atmos.*

534   *Chem. Phys.*, 2010;10:10399–420.

535 Loeb, N. G., and G. L. Schuster (2008), An observational study of the relationship between

536   cloud, aerosol and meteorology in broken low-level cloud conditions, *J. Geophys. Res.*, 113,

537   D14214, doi:10.1029/2007JD009763.

538 Lyapustin, A. and Y. Kaufman (2001), The role of adjacency effect in the optical remote sensing

539   of aerosol *J Geophys Res*, *106*: 11909-11916.

540 Marshak, A., A. Davis, W. Wiscombe, and R.F. Cahalan (1995), Radiative smoothing in fractal

541   clouds *J. Geophys. Res. (Atmos.)*, *100*, 26247-26261

542 Marshak, A., G. Wen, J. Coakley, L. Remer, N.G. Loeb, and R.F. Cahalan (2008), A simple

543   model for the cloud adjacency effect and the apparent bluing of aerosols near clouds *J.*

544   *Geophys. Res.*, *113*(D14S17) doi:10.1029/2007JD009196.

545 Marshak, A., K.F. Evans, T. Várnai, and G. Wen (2014), Extending 3D near-cloud corrections

546   from   shorter   to   longer   wavelengths   *J. Quant. Spec. Rad. Trans*, *147*, 79-85,

547   doi:10.1016/j.jqsrt.2014.05.022.

548 Martins, J. V., D. Tanré, L. Remer, Y. Kaufman, S. Mattoo, and R. Levy (2002), MODIS Cloud

549   screening for remote sensing of aerosols over oceans using spatial variability, *Geophys. Res.*

550   *Lett.*, 29(12), doi:10.1029/2001GL013252.

551 Odell, A. P. and J. A. Weinman, (1979), The effects of atmospheric haze on images of the

552   Earth's surface, *J. Geophys. Res.*, 80(36),5035-5040, doi:10.1029/JC080i036p05035.

553 Otterman, J. and R. S. Fraser (1979), Adjacency effects on imaging by surface reflection and

554   atmospheric scattering: cross radiance to zenith, *Appl. Opt.*, 18, 2852-2860, doi:

555   10.1364/AO.18.002852.

556 Pincus, R. and B. Stevens (2009), Monte Carlo spectral integration: A consistent approximation

557   for radiative transfer in large eddy simulations, *Journal of Advances in Modeling Earth*

558   *System*, June 2009, doi:10.3894/JAMES.2009.1.1.

559 Platnick, S., M. King, S. Ackerman, et al. (2003), The MODIS cloud products: Algorithms and

560   examples from Terra, *IEEE Trans Geosci Remote Sens*, **41 (2):** 459-473.

561 Redemann, J., Q. Zhang, P. B. Russell, J. M. Livingston, and L. A. Remer (2009), Case Studies

562   of Aerosol Remote Sensing in the Vicinity of Clouds, *J. Geophys. Res.*, 114, D06209,

563   doi:10.1029/2008JD010774.

564 Remer, L.A., Y.J. Kaufman, D. Tanre, S. Mattoo, D.A. Chu, J.V. Martin, R.-R. Li, C. Ichoku,

565   R.C. Levy, R.G. Kleidman, T.F. Eck, E. Vermote, and B.N. Bolben (2005), The MODIS

566   Aerosol Algorithm, Products, and Validation, *J. Geophy. Res.*, Vol 62, 947-973.

567 Rienecker, M.M., M.J Suarez, R. Gelaro, R. Todling, J. Bacmeister, E. Liu, et al. (2011),

568   MERRA:NASAs modern-era retrospective analysis for research and applications, *J. Clim.*,

569   24:3624–48.

570   Su, W., G. L. Schuster, N. G. Loeb, R. R. Rogers, R. A. Ferrare, C. A. Hostetler, J. W. Hair, and

571   M. D. Obland (2008), Aerosol and cloud interaction observed from high spectral resolution

572   lidar data, *J. Geophys. Res.*, 113, D24202,doi:10.1029/2008JD010588.

573   Stevens, B., C.-H. Moeng, P. P. Sullivan (1999), Large-Eddy Simulations of radiatively driven

574   convection: sensitivities to the representation of small scales, *J. Atmos. Sci.*, 56:3963-84.

575   Tackett, J. L. and L. Di Girolamo (2009), Enhanced aerosol backscatter adjacent to tropical trade

576   wind clouds revealed by satellite-based lidar, *Geophys. Res. Lett.*, 36, L14804,

577   doi:10.1029/2009GL039264.

578   Twohy, C. H., J. A. Coakley Jr., and W. R. Tahnk (2009), Effect of changes in relative humidity

579   on aerosol scattering near clouds, *J. Geophys. Res.*, 114, D05205,

580   doi:10.1029/2008JD010991.

581   Titov, G. A. (1990), Statistical description of radiation transfer in clouds, *J. Atmos. Sci.*, 47, 24 −

582   38, doi:10.1175/1520-0469(1990)047<0024:SDORTI>2.0.CO;2.

583   Várnai, T. and A. Marshak (2011), Global CALIPSO observations of aerosol changes near

584   clouds, *Geosci. Remote Sens. Lett. 19-23*, *8, Issue 1*, 19-23

585   doi:10.1109/LGRS.2010.2049982.

586   Varnai, T. and A. Marshak (2012) Analysis of co-located MODIS and CALIPSO observations

587   near clouds *Atmos Meas Tech*, *5*(2): 389-396, doi:10.5194/amt-5-389-2012.

588   Varnai, T. and A. Marshak (2014), Near-cloud aerosol properties from the 1 km resolution

589   MODIS ocean product *J. Geophys. Res. Atmos.*, *119*(3): 1546-1554

590   doi:10.1002/2013JD02063.

591 Vermote, E.F., D. Tanre, J. L. Deuze, M. Herman, and J.-J. Morcrette (1997), Second simulation

592   of the satellite signal in the solar spectrum, 6S: an overview, *IEEE Trans. Geosci. Remote*

593   *Sens.* 35, 675–686.

594 Wen, G., A. Marshak, R. F. Cahalan, L. A. Remer, and R. G. Kleidman (2007), 3-D aerosol-

595   cloud radiative interaction observed in collocated MODIS and ASTER images of cumulus

596   cloud fields, *J. Geophys. Res.*, 112, D13204, doi:10.1029/2006JD008267.

597 Wen, G., A. Marshak, and R.F. Cahalan (2008), Importance of Molecular Rayleigh Scattering in

598   the Enhancement of Clear Sky Radiance in the Vicinity of Boundary Layer Cumulus Clouds,

599   *J. Geophys. Res.*, 133(D24207)doi:10.1029/2008JD010592.

600 Wen, G., A. Marshak, R. C. Levy, L. A. Remer, N. G. Loeb, T. Várnai, and R. F. Cahalan

601   (2013), Improvement of MODIS aerosol retrievals near clouds, *J. Geophys. Res. Atmos.*, 118,

602   9168–9181, doi:10.1002/jgrd.50617.

603 Yang, Y., and L. Di Girolamo (2008), Impacts of 3-D radiative effects on satellite cloud

604   detection and their consequences on cloud fraction and aerosol optical depth retrievals, *J.*

605   *Geophys. Res.*, 113, D04213, doi:10.1029/2007JD009095.

606 Yang, W., Marshak, A., Varnai, T., Wood, R. 2014. CALIPSO observations of near-cloud

607   aerosol properties as a function of cloud fraction, *Geophys. Res. Lett, 41*: 9150-9157,

608   doi:10.1002/2014GL061896.

609 Zhuravleva, T., and A. Marshak (2005), On the validation of the Poisson model of broken

610   clouds, *Izv. Atmos. Oceanic Phys.*, 41(6), 713– 725.

611

612 **Figures**
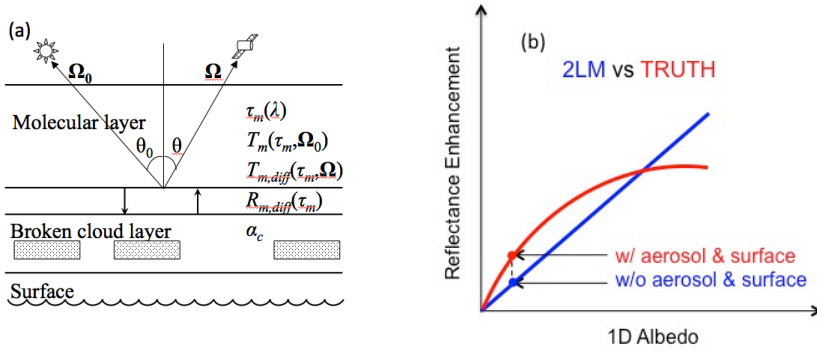
613

614 Fig. 1. (a) A sketch of the 2LM showing directions of the Sun ($\mathbf{\Omega_0}$) and satellite ($\mathbf{\Omega}$), solar zenith
615 angle (θ_0) and satellite viewing zenith angle (θ), properties of the molecular layer (i.e., τ_m:
616 molecular scattering optical depth, T_m: transmittance of solar radiation from above, $T_{m,diff}$:
617 transmittance of diffuse radiation from below, $R_{m,diff}$: reflectance of diffuse radiation from
618 below) for MODIS aerosol wavelength λ, and cloud albedo (α_c) (*Marshak et al.*, 2008). (b) A
619 sketch of the characteristics of 2LM estimated reflectance enhancement versus the truth.

620

621
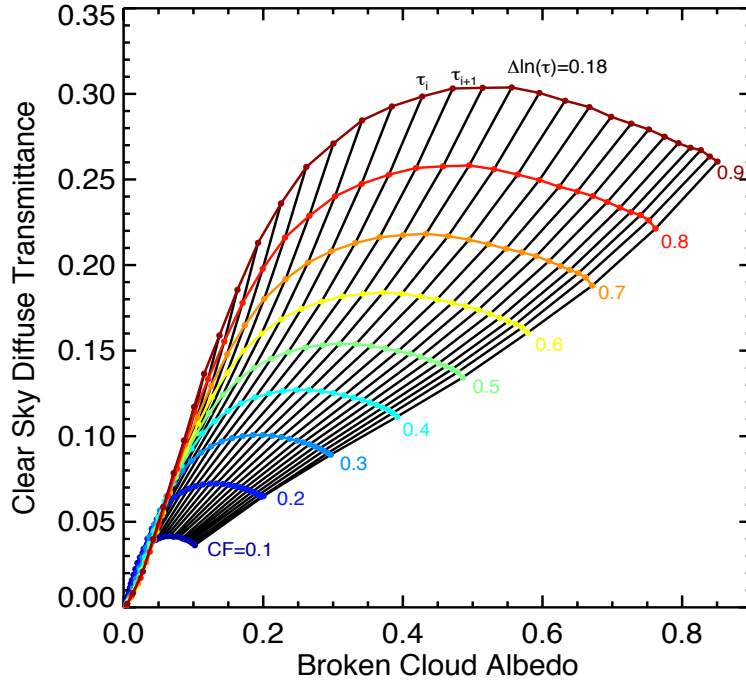
622 Fig. 2. Clear sky diffuse transmittance as a function of cloud albedo for different cloud fractions
623 (color lines) and average cloud optical depths (black lines). Cloud aspect ratio (*D/H*) is 2 and
624 SZA=36°. The cloud fraction ranges from 0.1 to 0.9 with increments of 0.1. The cloud optical
625 depth ranges from 0.1 to 158, where $\Delta\tau = 0.25$ for $\tau \leq 2$, and $\Delta\ln(\tau)=0.18$ for $\tau > 2$. Here $\tau_i =$
626 10.3, $\tau_{i+1} = 12.36$.

627

628
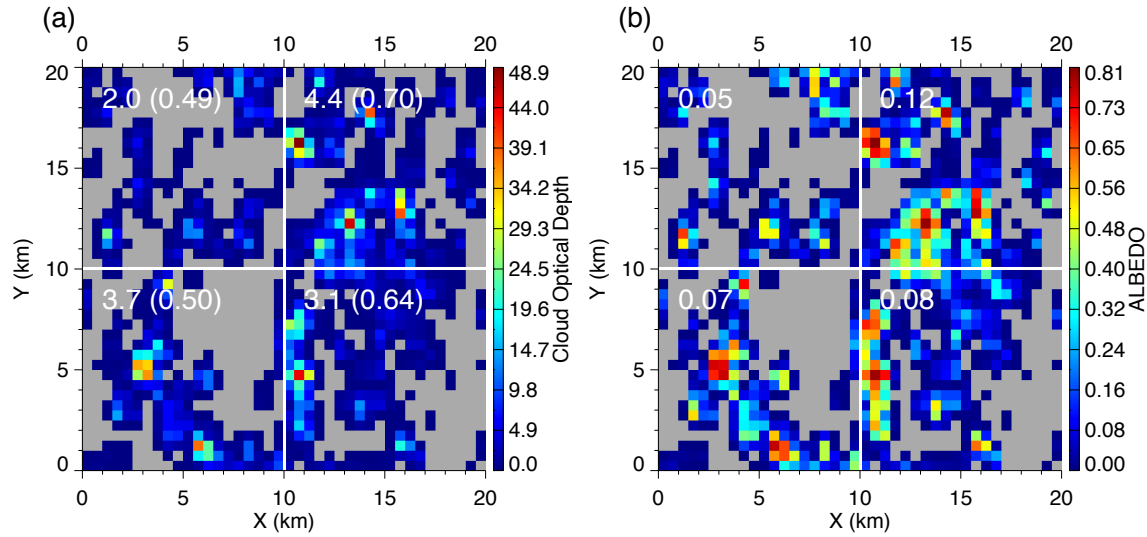
629
630 Fig. 3. (a): An example of the LES-simulated 20 km x 20 km cloud optical depth field with grey
631 color for clear (mean optical depth of cloudy pixels is 3.4 and cloud fraction is 0.58). Average
632 optical depth for cloudy pixels and cloud fraction (in parenthesis) are indicated for each 10 km x
633 10 km box. (b): 1D cloud albedo for the cloud field in the left panel with SZA = 26.1°. Albedo of
634 clear pixels in grey is zero. Domain average albedo over cloudy and clear pixels is 0.079. The
635 average albedo for each 10 km x 10 km box is indicated.

636

637
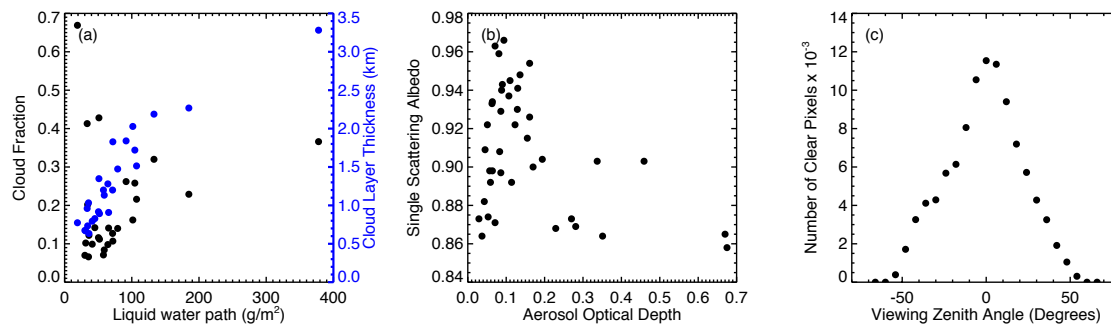
638
639 Fig. 4. Cloud and aerosol properties of LES simulated cumulus cloud fields. (a) cloud fraction
640 and cloud layer thickness as a function of liquid water path, (b) aerosol single scattering albedo
641 as a function of aerosol optical depth, (c) clear pixels identified by the MOD04 mask as a
642 function of viewing zenith angle.

643

644

645
646
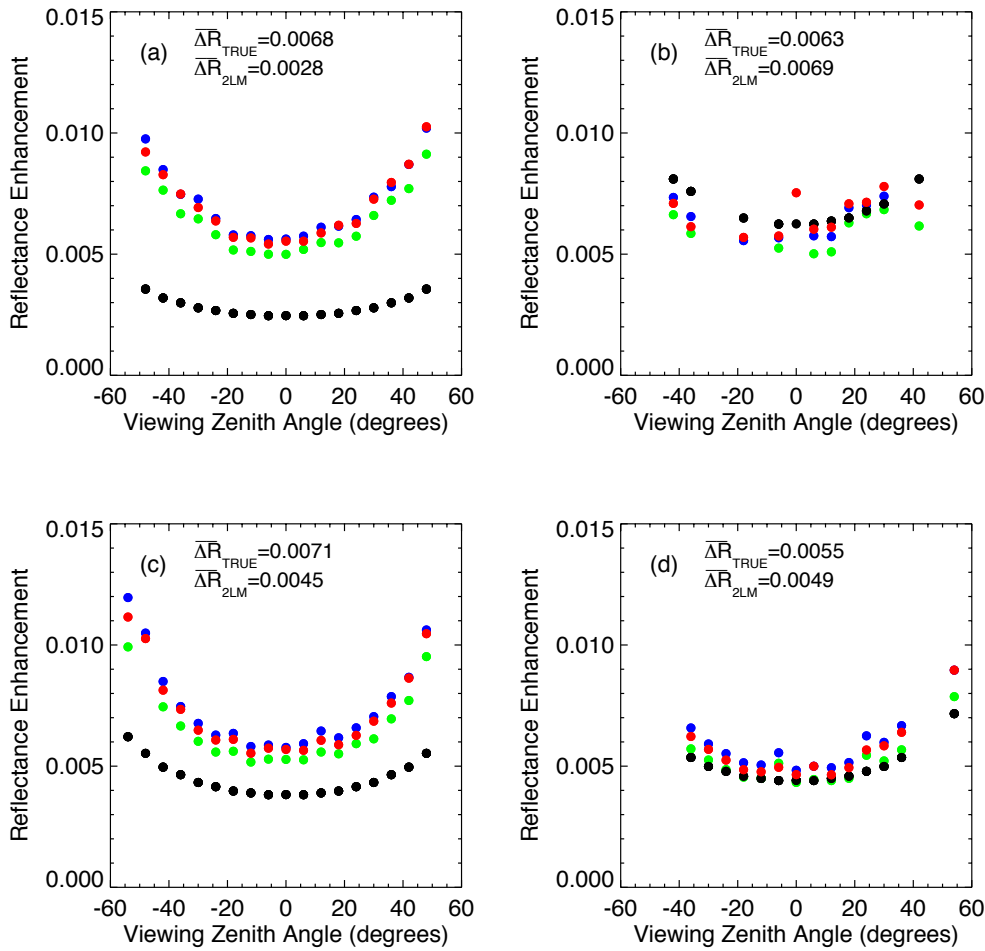
Fig. 5. Reflectance enhancement as a function of viewing zenith angle for the 2LM estimates (black dots) and the truth (color dots) for the four 10 km x 10 km sub-images in Fig. 4a. For the truth, three aerosol profiles with AOD of 0.045, 0.083, 0.194 are indicated by green, blue, and red, respectively. The average of all reflectance enhancements of 2LM is 0.0045 compared to the truth of 0.0065.

652
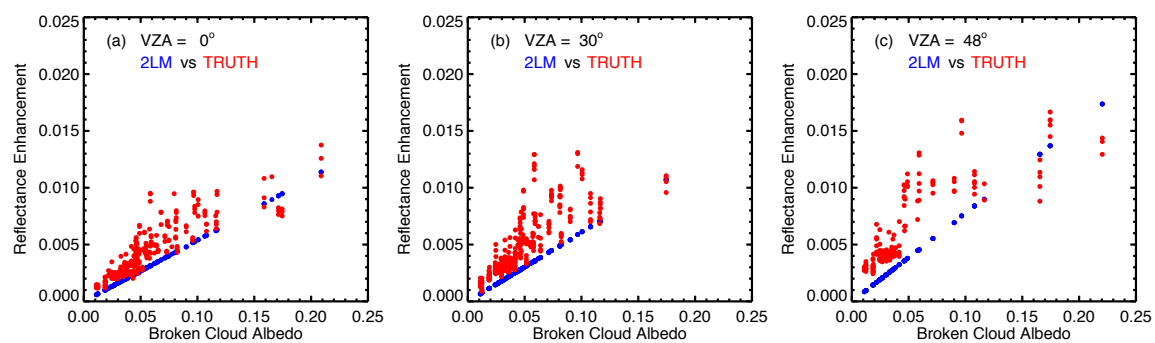
653
654 Fig. 6. Compare 2LM reflectance enhancements (blue) with the truth (red) for (a) nadir, (b)
655 oblique view-angles for all cloud scenes.

656
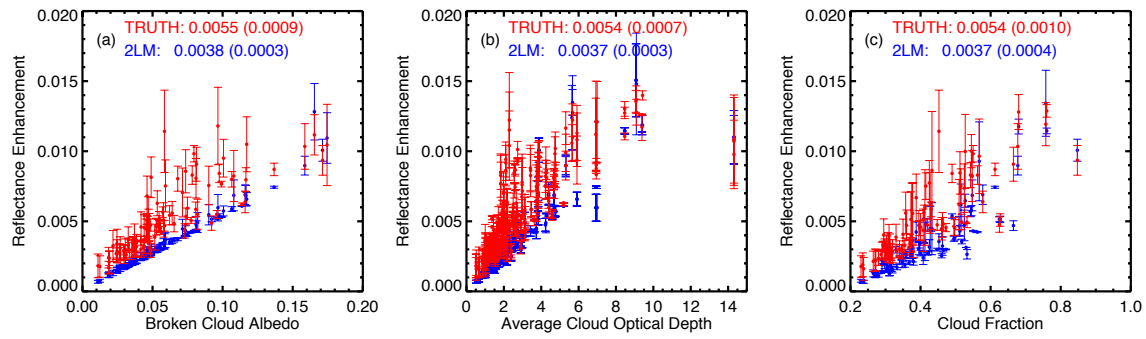
657
658 Fig. 7. 2LM estimated reflectance enhancement (red) and the truth (blue) as a function of (a)
659 cloud albedo, (b) cloud optical depth, and (c) cloud fractions. The mean values of average
660 enhancement and standard deviation (in parentheses) are indicated.

661

662
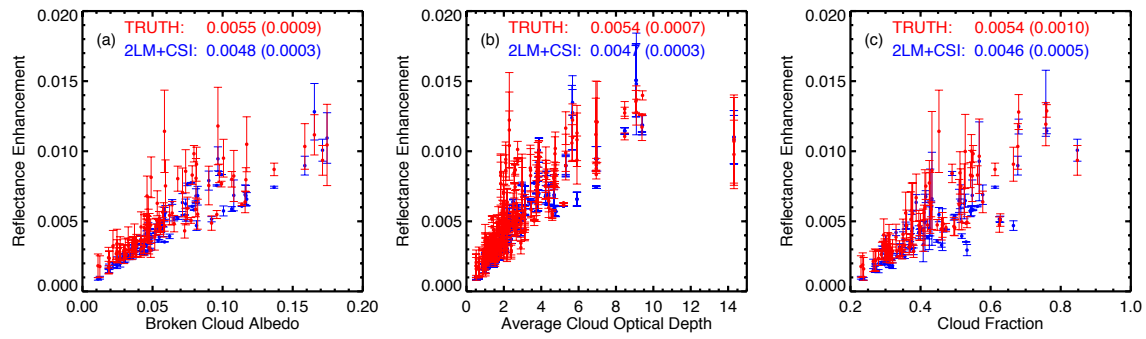
663
664 Fig. 8. Similar to Fig. 7 but the red for 2LM+CSI estimated reflectance enhancements.

665

666
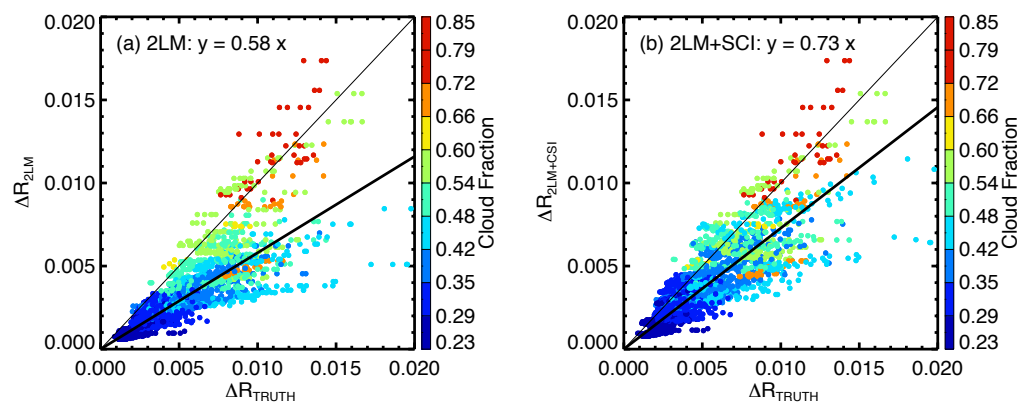
667 Fig. 9. Compare (a) 2LM and (b) 2LM+CSI estimated reflectance enhancements with the truth
668 with cloud fraction indicated by colors. Increase of the slope as model includes more physical
669 mechanism is evident.

670
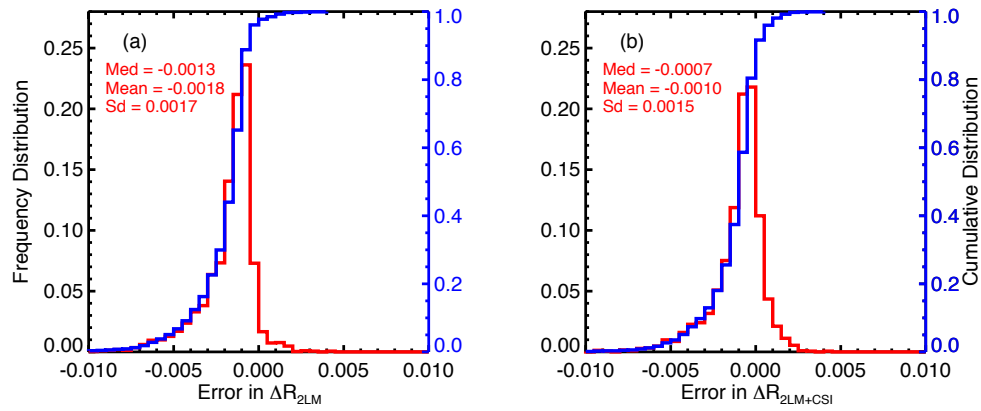
Fig. 10. Distributions of errors in modeled reflectance enhancement (a) for 2LM and (b) for 2LM+CSI with median (Med), mean (Mean), and standard deviation (Sd) indicated. For the true mean reflectance enhancement (Fig. 11), mean errors are -36% and -20% for 2LM and 2LM+CSI, respectively.
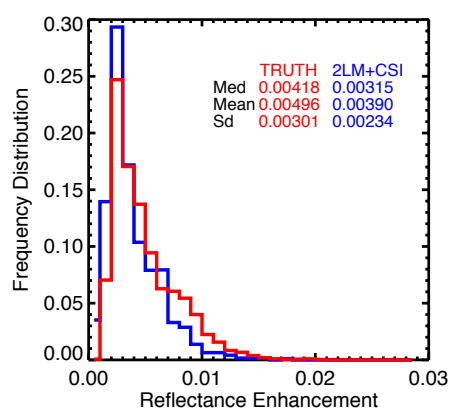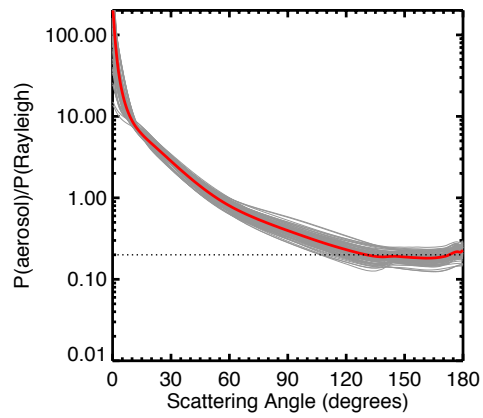
677

Fig. 11. Distributions of 2LM+CSI (blue) and the true (red) reflectance enhancement with median (Med), mean (Mean), and standard deviation (Sd) indicated.
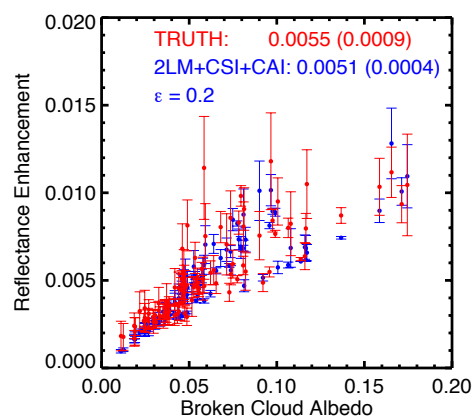
680

681

682

Fig. 12. The ration of aerosol scattering phase function to Rayleigh scattering phase function for the 40 different aerosols (grey) in LES/SHDOM simulations and average value (red).

685

686

Fig. 13. Similar to Fig. 8a but with additional cloud-aerosol interactions assuming ε = 0.2.